ACS OMEGA

Open Access

http://pubs.acs.org/journal/acsodf

Article

Evaluation of Nanostructured NiS_2 Thin Films from a Single-Source Precursor for Flexible Memristive Devices

Trishala R. Desai, R. Sai Prasad Goud, Tukaram D. Dongale, and Chitra Gurnani*

Cite This: *ACS Omega* 2023, 8, 48873−48883

Read Online

ACCESS | Metrics & More | Article Recommendations | Supporting Information

ABSTRACT: Herein, we report the first demonstration of a single-step, *in situ* growth of NiS_2 nanostructures from a single-source precursor onto a flexible substrate as a versatile platform for an effective nonvolatile memristor. The low temperature, solution-processed deposition of NiS_2 thin films exhibits a wide band gap range, spherical-flower-like morphology with high surface area and porosity, and negligible surface roughness. Moreover, the fabricated Au/NiS_2/ITO/PET memristor device reveals reproducible bipolar resistive switching (RS) at low operational voltages under both flat and bending conditions. The flexible device shows stable RS behavior for multiple cycles with a good memory window ($\sim 10^2$) and data retention of up to 10^4 s. The switching of a device between a high-resistance state and a low-resistance state is attributed to the filamentary conduction based on sulfur ion migration and sulfur vacancies and plays a key role in the outstanding memristive performance of the device. Consequently, this work provides a simple, scalable, solution-processed route to fabricate a flexible device with potential applications in next-generation neuromorphic computing and wearable electronics.

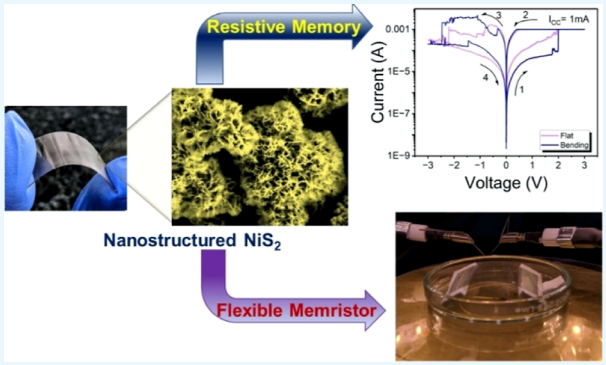

1. INTRODUCTION

Flexible electronic devices with robust bending stability have attracted much attention due to their applications in bionic sensors,[1,2] memory,[3] and human−machine interfaces.[4] Moreover, the advances in sensor technology, intelligent algorithms, and integrated circuits have propelled human−computer interaction to the forefront of innovation.[5,6] Consequently, there is a need for the development of flexible electronic systems with low energy consumption and potential scope in the areas of computation. In conventional computing systems, the major cause for energy consumption arises from the von Neumann architecture where the computing units are separated from memory units leading to huge energy loss while shuffling data.[7] The new computing paradigm based on memristor with in-memory computing is an alternative to the von Neumann computing system and a prominent candidate for the next generation of memory and neuromorphic computing applications.[8,9] The resistive switching (RS) phenomena of the memristive device with metal−insulator−metal (MIM) structure rely on the change in the resistance of the active layer material sandwiched between the two metal electrodes.[10,11] Under the influence of an applied electric field, the resistance of the active layer material can alternate between the high-resistance state (HRS) and the low-resistance state (LRS) to store data.[12] Unfortunately, the majority of memristors are built on conventional silicon substrates which are not suitable for flexible electronic applications. As a result, it is crucial to investigate novel nanomaterials that combine state-of-the-art flexible memristors with high performance, nonvolatile RS behavior along with scalability and industrially acceptable processing.

The low-dimensional (layered) transition metal dichalcogenides (TMDCs) are attractive candidates for future electronics due to their tunable band gap, transparency, flexibility, and ability to downscale to atomic level in material size and thickness.[13] They are particularly interesting as switching materials for memristor devices and future low-power neuromorphic computing. Compared with commonly investigated metal oxides, metal chalcogenides (S, Se, and Te) feature a shallow energy landscape due to softer chemical bonds (i.e., lower cohesive energy) and the physical and chemical origins of electronic transitions in chalcogenide-based materials can be more energy efficient.[14] In addition, TMDCs offer easily accessible surfaces that can be used to control electronic transitions by external inputs.[15]

Moreover, the large-scale deposition of nanostructured TMDCs on flexible substrates has never been straightforward due to limitations in current deposition methods such as

Received: August 25, 2023
Revised: October 18, 2023
Accepted: November 8, 2023
Published: November 21, 2023

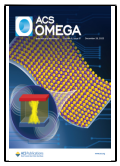

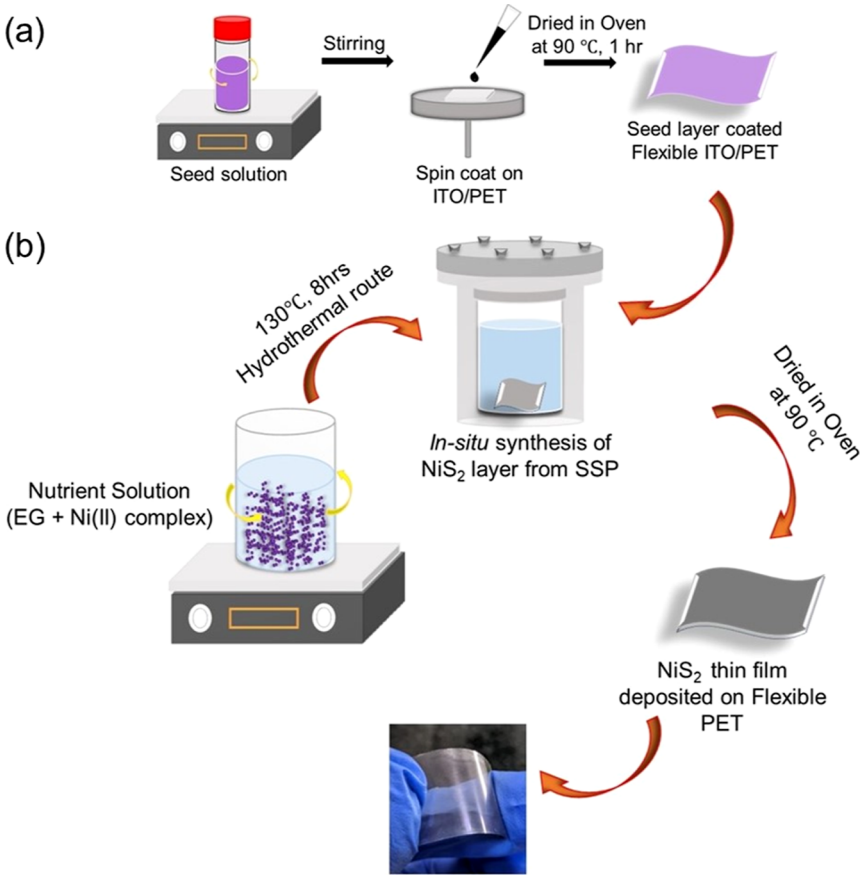

Figure 1. Graphical illustration of the *in situ* growth of NiS_2 layer using SSP on flexible ITO/PET substrate. (a) Seed layer deposition by spin coat technique and (b) growth of NiS_2 using the solvothermal route.

exfoliation and chemical vapor deposition (CVD). The promising performance of flexible memristors has been demonstrated on a few layers of TMDCs using an assembly of small flakes exfoliated from crystals and transferred onto target substrates,[16,17] a process that is not compatible with large-scale manufacturing. CVD[18] and physical epitaxy[19] show promising scalability; however, their high deposition temperatures are not compatible with the thermal budget of most of the potential flexible substrates. Although a film transfer process could be adapted to integrate those films onto flexible substrates, the size is limited to a centimeter scale.[20] Solution processable methods have a number of key distinguishing features. It enables low-temperature processing, easy stoichiometric modulations, eco-friendly, high throughput production, and good compatibility with roll-to-roll manufacturing and printing techniques.[21] Specifically, the low thermal solution processable technique avoids the deformation of polymer substrates like PET and polyimides. This makes solution-processing techniques key to the next generation of flexible and wearable electronics. Many of the potential flexible electronics are limited by the lack of availability of mass manufacturing of low-dimensional chalcogenides. Among these methods, the in situ solvothermal approach serves as the better alternative for the synthesis of metal sulfide nanostructures from single-source precursors (SSP), which have the potential advantages of relatively low cost, high purity, and controlled morphology.[22] Using single-source precursors has its own advantages over those of its dual-source counterparts. The outstanding properties of the precursors such as ease of handling and compatibility with solvents enable binder-free deposition without using toxic stabilizers and reducing agents. Furthermore, the earth-abundant nickel sulfide has attracted much interest among the family of metal sulfides due to its various stoichiometries[23] (NiS, Ni_3S_2, Ni_3S_4, Ni_6S_5), high electron mobility and unique metal−insulator properties.[24] Consequently, it is widely studied as an electrode material for energy storage devices such as supercapacitors,[25] and also a potential competitor for silicon in thin film solar cells.[26] However, the role of nanostructured nickel disulfide (NiS_2) as the RS material for flexible resistive random access memory (ReRAM) applications remains unexplored.

In this work, we demonstrate the novel, single-step, *in situ* growth of NiS_2 nanostructures on a flexible substrate from the single-source precursor $[Ni\{S_2P(OPr)_2\}_2]$ at low temperatures using a solution-processable, solvothermal route. The as-fabricated NiS_2 nanostructure-based flexible device acts as an excellent RS memory. In particular, the developed device exhibits bipolar RS with a stable memory window under the applied direct current (DC) voltage sweep including better-switching repeatability and mechanical stability. This work opens up new avenues for simple, scalable, and cost-effective devices for flexible electronics.

2. MATERIALS AND METHODS

2.1. Materials. Nickel chloride ($NiCl_2{\cdot}6H_2O$) and phosphorus pentasulfide (P_2S_5) were purchased from Sigma-Aldrich. Toluene (99.5%, bp 110.6 °C), propanol (Pr-99%, bp 97 °C), benzene, and ethylene glycol were procured from S D

https://doi.org/10.1021/acsomega.3c06331
ACS Omega 2023, 8, 48873−48883

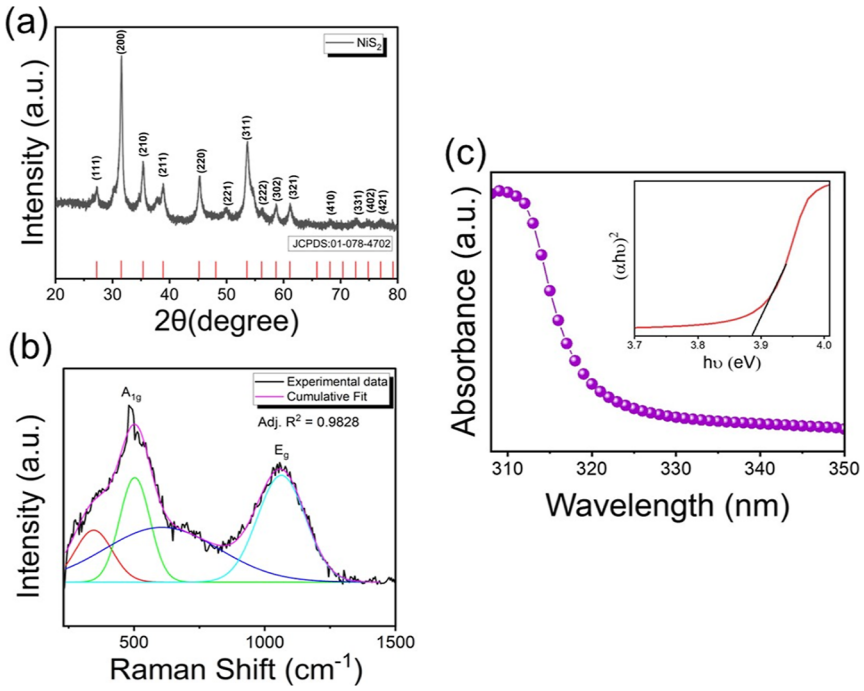

Figure 2. (a) XRD and (b) Raman spectra of NiS_2. (c) Absorption spectra with a band gap analysis of NiS_2 on a flexible substrate (ITO/PET).

Fine-chem Limited. All chemicals were of analytical grade. The solvents (toluene and benzene) were dried and distilled by the standard methods before use. The reactions were performed in Schlenk and vacuum lines, and precautions were taken to avoid moisture during experimental manipulations. ITO/PET (indium tin oxide layer coated on polyethylene terephthalate) was purchased from Sigma-Aldrich.

2.2. Synthesis of Single-Source Precursor. The single-source precursor $[Ni\{S_2P(OPr)_2\}_2]$ was synthesized from a metathesis reaction of ammonium salts of *O*,*O*′-dipropyl dithiophosphates and $NiCl_2{\cdot}6H_2O$ in a 2:1 molar ratio.[27] The purple solid was further characterized by IR, ^1H, and $^{31}P\{^1H\}$ NMR spectroscopy. Yield: (0.96 g) 88.88%; IR (KBr): 983b, 856s, 752s, 642s, 547s cm^{-1}; $\{^1H\}$ NMR ($CDCl_3$, 298k, δ ppm): 4.19 (dd, [4H], *o*−CH_2), 1.78 (m, [4H], −CH_2CH_3), 1.00 (t, [6H], −CH_3); ^{31}P ($CDCl_3$, 298k, δ ppm): 92.95 (s).

2.3. Direct Growth of NiS_2 Thin Films on Flexible Substrate Using SSP. *In situ* growth of nickel disulfide on the flexible ITO/PET substrate was performed under the low temperature, solution-processable, solvothermal route as illustrated in Figure 1. Initially, the seed solution was prepared by dissolving $[Ni\{S_2P(OPr)_2\}_2]$ complex (50 mg) in 1 mL of benzene, and the solution was spin-coated at 3000 rpm onto the cleaned ITO/PET substrate. Further, the seed layer-coated ITO/PET substrate was dried in an oven at 90 °C for 1 h (Figure 1a). Next, the nutrient solution was prepared by dispersing 0.161 g (0.7 mmol) of $[Ni\{S_2P(OPr)_2\}_2]$ in 20 mL ethylene glycol, and the mixture was stirred continuously for 1 h at R.T. After stirring, the suspension was transferred to a 25 mL Teflon liner and the seed layer-coated ITO/PET was placed upside down inside the solution as shown in Figure 1b. The autoclave reactor was packed tightly and moved to the furnace, and the temperature was maintained at 130 °C for 8 h. After the reaction, the autoclave was allowed to cool to room temperature. Further, the deposited film was rinsed twice with deionized water. Finally, the obtained film was dried in a vacuum oven at 80 °C for 2 h.

2.4. Fabrication and Measurements of Au/NiS_2/ITO/PET Flexible Memristor. The device was fabricated using the solvothermal grown NiS_2 as the active layer and the flexible ITO-coated PET (2 × 2 cm^2) acts as the bottom electrode. The thickness of the active layer was measured to be ∼8.01 μm. Finally, the top circular Au electrodes (thickness ∼100 nm and 0.2, 0.5- and 1 mm radius) were patterned on the NiS_2/ITO layer by the shadow mask-assisted thermal evaporation technique. Overall, the Au/NiS_2/ITO/PET device was fabricated by a simple and cost-effective route. The electrical measurements of the fabricated flexible device were measured using a B1500A Semiconductor Device Parameter Analyzer with PE4 Probe System.

2.5. Material Characterization. The infrared spectra were recorded using an Alpha Bruker FTIR spectrometer in the range of 400−1200 cm^{-1}. A Bruker Avance NEO NMR spectrophotometer (500 MHz) was used for the (^1H and ^{31}P) NMR measurement in $CDCl_3$. RIGAKU Smartlab instrument (λ = 1.54) with a kα filter was used at room temperature to confirm the crystalline phases of samples. The Raman spectra were recorded using a Raman spectrometer (Bruker Multi-RAM) in the range of 120−1700 cm^{-1} at the excitation wavelength of 514 nm. The absorbance and transmittance spectra were recorded from the 200−1000 nm range using UV−vis spectroscopy (Cary 5000, Varian, USA). The surface morphology and topology of the as-synthesized NiS_2 nanostructures were studied using a scanning electron microscope (SEM) (JEOL-JSM 6360A) and the atomic force microscopy (Asylum RESEARCH AFM MFP-3D) in tapping mode/AC mode and tapping frequency 300 kHz, respectively.

3. RESULTS AND DISCUSSION

3.1. Precursor Characterization. The purity and composition of the complex was confirmed from the IR, ^1H, and $^{31}P\{^1H\}$ NMR spectra as shown in Figures S1−S3, respectively. The five important vibrational bands are observed in the IR spectra of the $[Ni\{S_2P(OPr)_2\}_2]$ complex (Figure

https://doi.org/10.1021/acsomega.3c06331
ACS Omega 2023, 8, 48873−48883

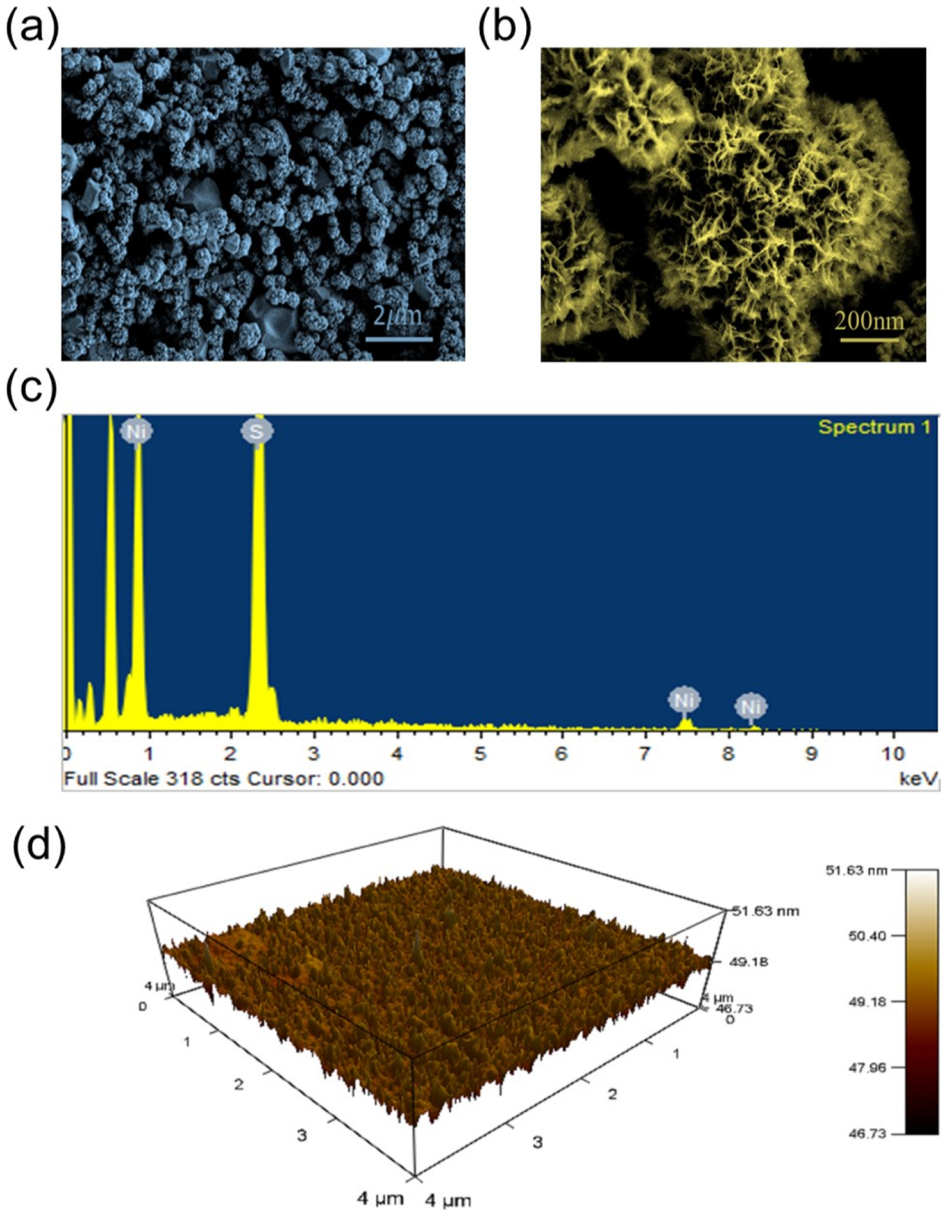

Figure 3. SEM images of NiS_2 nanoflowers with different magnifications such as (a) 2 μm, (b) 200 nm, and (c) EDS spectrum. (d) AFM image of the NiS_2/ITO thin film on a flexible substrate (PET).

S1). Two strong intensity bands observed at 983 and 856 cm^{-1} correspond to the ν(P)−O−C and ν P−O−(C) stretching vibrations. While the band at 752 and 642 cm^{-1} corresponds to ν(P−O) and ν(P═S) vibrations and shows a slight shift toward lower wavenumber in comparison with $[NH_4][(OC_3H_7)_2S_2P]$. The Ni−S bond is observed in the far IR region at 547 cm^{-1} which confirms the coordination of metal with *O*,*O*′-dipropyl dithiophosphates. The $^1\{H\}$ (Figure S2) and $^{31}P\{^1H\}$ (Figure S3) NMR spectra for the $[Ni\{S_2P(OPr)_2\}_2]$ complex were recorded in $CDCl_3$ at room temperature. The $^1\{H\}$ spectrum is compared to the spectrum of ammonium salts of dithiophosphoric acids $[NH_4][(OC_3H_7)_2S_2P]$. In the complex, the $-CH_3$ protons observed as multiplets, resonating in the region of 1.00−4.19 ppm, show the coordination shift of 0.6 ppm associated with those of corresponding ammonium salts. The $^{31}P\{^1H\}$ NMR spectra of the complex display a sharp singlet peak at 92.95 ppm, indicating the presence of a pure single form of phosphorus and coordination of the dithiophosphate group with the nickel center in the molecule. The $^{31}P\{^1H\}$ NMR chemical shift for this complex is 18 ppm upfield from that of the ammonium salts of dithiophosphoric acids.

3.2. Solution-Processed *In Situ* Growth of Nanostructured NiS_2 Thin Films. The NiS_2 thin film was deposited by a simple, solution-processable solvothermal route using single-source precursor $[Ni\{S_2P(OPr)_2\}_2]$. The commonly used dual source techniques with high deposition temperatures are not compatible with the thermal budget of most of the flexible substrates including PET. Therefore, the *in situ* solvothermal route based on SSPs serves as an alternative low-temperature solution process method. The amazing versatility of dithiophosphate complexes as SSPs stems from their ease of handling, high shelf life, and relative stability of metal complexes. Moreover, $[Ni\{S_2P(OPr)_2\}_2]$ contains a preformed Ni−S bond which decomposes even at low temperatures in the solution phase,[28] and the ethylene glycol[29]

https://doi.org/10.1021/acsomega.3c06331
ACS Omega 2023, 8, 48873−48883

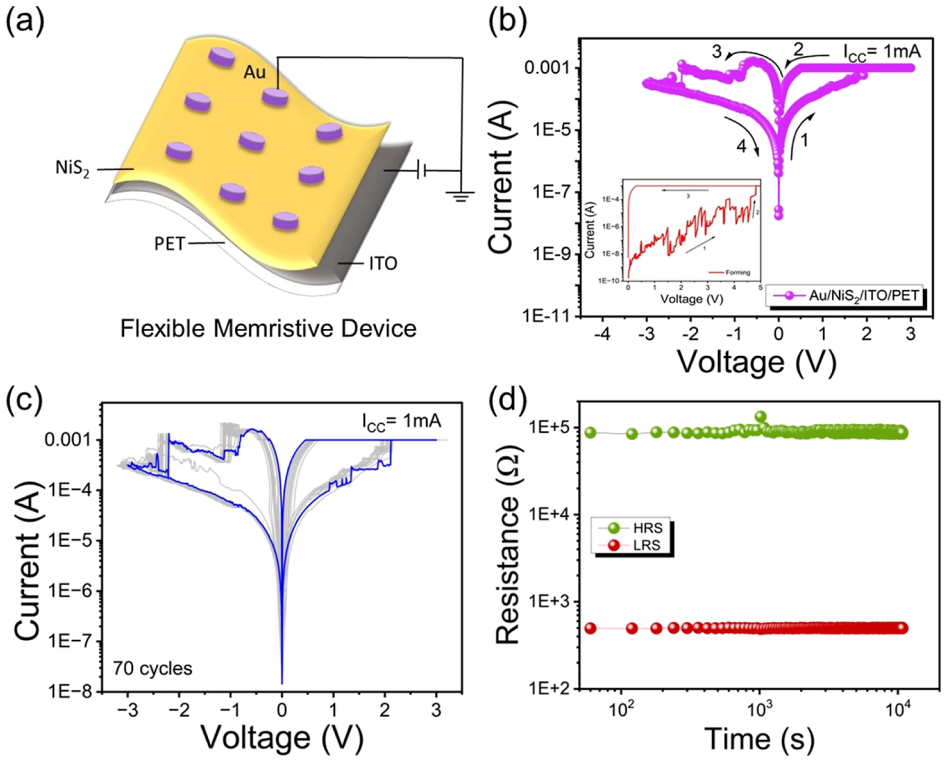

Figure 4. (a) Schematic model illustrating the flexible Au/NiS_2/ITO/PET device structure. (b) Bipolar $I-V$ characteristics (inset electroforming process) of the Au/NiS_2/ITO/PET device. (c) Multiple $I-V$ cycles. (d) Data retention characteristics of the flexible Au/NiS_2/ITO/PET memristor device.

as solvent controls the particle size and homogeneity of nanostructures resulting in the formation of low dimensional nickel disulfides. Thus, the novel solution-processed method enables a high-quality (pure, uniform, well-adhered) NiS_2 thin film to be deposited on a flexible substrate at a low temperature.

3.3. Structural and Morphological Studies of Nanostructured NiS_2 Thin Film. *3.3.1. X-ray Diffraction Studies.* The X-ray diffraction (XRD) spectra of the as-synthesized NiS_2 thin films were recorded to study the crystallinity and phase structure. The sharp diffraction peaks observed in the XRD pattern (Figure 2a) indicate the crystalline nature of the as-synthesized NiS_2. All the diffraction peaks containing (111), (200), (210), (211), (220), (221), (311), (222), (302), (321), (410), (331), (402), and (421) faces in this pattern well matched with the JCPDS reference no. 01-078-4702 with lattice constants of $a = b = c = 5.66$ Å and can be indexed to the pure cubic structure of the NiS_2 phase. No additional peaks of any other form of nickel sulfide were observed indicating the purity of NiS_2 from single molecular precursors.[30] The average particle size was calculated using the Debye–Scherrer formula and is found to be around 54.71 nm.

3.3.2. Raman Spectral Studies. Raman spectra of the as-synthesized NiS_2 layer were studied to analyze the crystalline structure of the sample. Figure 2b shows the deconvoluted Raman spectra of the NiS_2 layer fitted using the Lorentzian function. The band at 270, 480, 513, and 1051 cm^{-1} corresponds to the A_{1g} and E_g active modes of vibration of NiS_2.[31,32] As the Raman modes of vibration strongly depend on the crystal lattice vibrations, some of the vibration modes of bulk NiS_2 are not clearly observed due to the reduction in size of NiS_2 nanostructures.[33] Thus, the Raman peaks confirm the formation of single-phase NiS_2.

3.3.3. UV–Vis Spectroscopic Studies. Using UV–vis spectroscopy, the optical characteristics of the as-synthesized NiS_2 thin layer were investigated, and the band gap was determined using the Tauc equation:[34] $(\alpha h\upsilon)^n = B(h\upsilon - E_g)$, where E_g is the optical band gap, h is the Planck's constant, υ is the frequency of incident photon, α is absorption coefficient, B is a material constant, and n is 2 for direct transitions and 1/2 for indirect transitions. The optical absorption spectrum and Tauc plot for the band gap calculation (inset) are shown in Figure 2c. In comparison to bulk nickel sulfide, the as-synthesized NiS_2 layer absorbs maximum light in the UV region (200–350 nm). The observed blue shift can be attributed to the decrease in particle size and thus confirms the formation of nanosized nickel sulfide particles. This in turn increases the band gap of synthesized nanostructures.[35] The band gap of as-deposited NiS_2 thin layer was calculated as 3.87 eV. The linear relation is observed for $n = 2$ and, thus, the NiS_2 can be considered as a direct band gap semiconductor material. The transmittance spectrum of the NiS_2 layer on the flexible ITO/PET substrate was recorded in the range of 200–1000 cm^{-1} and was found to be more than 50% as shown in Figure S4. Therefore, the spherical flower-like morphology with high surface area and porosity, outstanding electrical characteristics such as the wide band gap range, and high dielectric strength of the as-synthesized NiS_2 thin films make it suitable for RS.

3.3.4. SEM Studies. The SEM images are acquired to better understand the morphology of the sample. Figure 3a,b shows the in situ growth of NiS_2 on a flexible substrate using $[Ni\{S_2P(OPr)_2\}_2]$ complex at low temperature, which confirms the spherical flower-like morphology and uniformity over the large surface area. In addition, the high magnification SEM image (Figure 3b) shows the high surface area and porous structure of the NiS_2 nanoflowers in the 50–100 nm

https://doi.org/10.1021/acsomega.3c06331
ACS Omega 2023, 8, 48873–48883

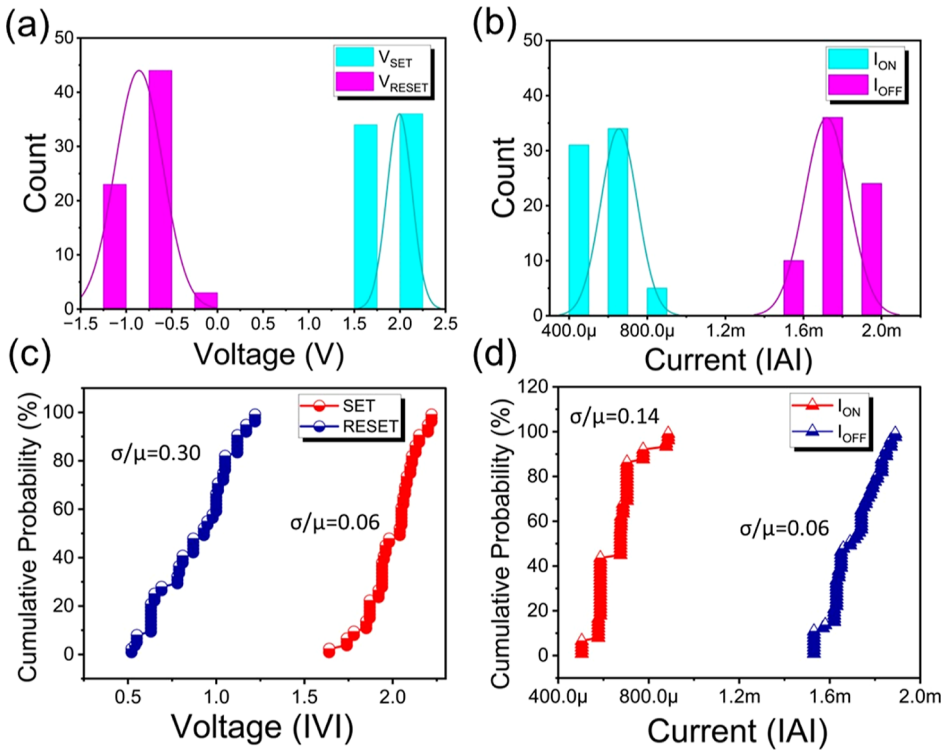

Figure 5. Statistical evaluation of the switching voltage and current of the flexible Au/NiS_2/ITO/PET memristor device. Histogram plots of (a) V_{SET} and V_{RESET} and (b) OFF and ON current distribution. Cumulative probability of (c) V_{SET} and V_{RESET} and (d) I (OFF) and I (ON).

size range. Furthermore, the EDS analysis of the sample was carried out to confirm the formation of pure NiS_2 from SSP. Figure 3c shows the EDS spectra of the NiS_2 nanostructures and the resulting peaks suggest the presence of nickel and sulfur with the atomic percentage of a 1:2 ratio which confirms the formation of NiS_2 via the hydrothermal route. Moreover, surface defects and roughness are the critical factors influencing the leakage current or unintended conduction pathways. Therefore, the as-deposited film texture was examined using an AFM. Figure 3d shows the AFM image of the NiS_2 thin film on the flexible substrate (PET). The demonstrated structure revealed a dense morphology and appeared as a uniform surface, which is consistent with the SEM data. The measured roughness is in the range of 49−53 nm for the selected area (4 × 4 μm).

3.4. Device Characterization. *3.4.1. Nanostructured NiS_2-Based Nonvolatile Flexible Memory Device.* The flexible device was fabricated in the form of a MIM structure with porous NiS_2 nanoflowers sandwiched between the Au top electrode and ITO-coated PET as the bottom electrode (Figure 4a). The electrical behavior and RS properties of the porous NiS_2 were studied from the current−voltage (I−V) characteristics. The semilogarithmic I−V plot of the Au/NiS_2/ITO/PET device shown in Figure 4b exhibited asymmetric, bipolar RS behavior, and the arrows indicate the switching direction. The device is initially subjected to a forming voltage of 5 V to cause a mild breakdown that can be regarded as electroforming. The I−V curves were then measured by sweeping the DC voltage from 0 V → +3 V → 0 V → −3 V→ 0 V with the compliance current of 1 mA in the positive voltage region and 50 mA in the negative voltage region. The compliance current limits the operating current and consequently prevents the breakdown of the device.[36] On application of positive DC sweep from 0 to +3 V, the device gradually switches from high to low resistance state (SET) at V_{SET} ∼ +2 V and RESET's back from low to high resistance state at V_{RESET} = −1.4 V during the reversal of polarity. This change in state is due to the formation and rupture of the filament within the switching layer. Further, to test the repeatability of the device, the I−V curves were recorded for multiple switching cycles, and the cycle-to-cycle performance of the as-fabricated device was investigated. The device exhibited reproducible and uniform switching behavior over 70 consecutive cycles (Figure 4c). Figure S5 shows the DC endurance of the fabricated device, where the device maintains a memory window (HRS/LRS) of ∼100. The data retention performance of the Au/NiS_2/ITO/PET device was studied by measuring the resistance states repeatedly (R_{ON} and R_{OFF}) for a longer duration of time at a read voltage of 0.4 V. Appreciably, the NiS_2-based device can retain data over 1 × 10^4 s without any interruption (Figure 4d).

Further, to evaluate the reliability and uniformity of our memristive device, the memory performance properties, including the histogram distribution (Figure 5a,b) and cumulative probability plots (Figure 5c,d), were studied for 70 consecutive switching cycles. Both curves depict the excellent uniformity of the switching performance with differentiating SET−RESET voltages and ON−OFF currents. To provide a quantitative comparison of all switching parameters, the coefficient of variation (σ/μ, σ is standard deviation, and μ is the mean value) was determined and is observed to be 0.06 and 0.30 for V_{SET} and V_{RESET}, respectively. Moreover, the coefficient of variation for LRS and HRS was also determined and is measured to be 0.14 and 0.06, respectively. These results reveal the narrow distribution of the operational voltage and current and demonstrate the excellent cycle-to-cycle uniformity of the device.

https://doi.org/10.1021/acsomega.3c06331
ACS Omega 2023, 8, 48873−48883

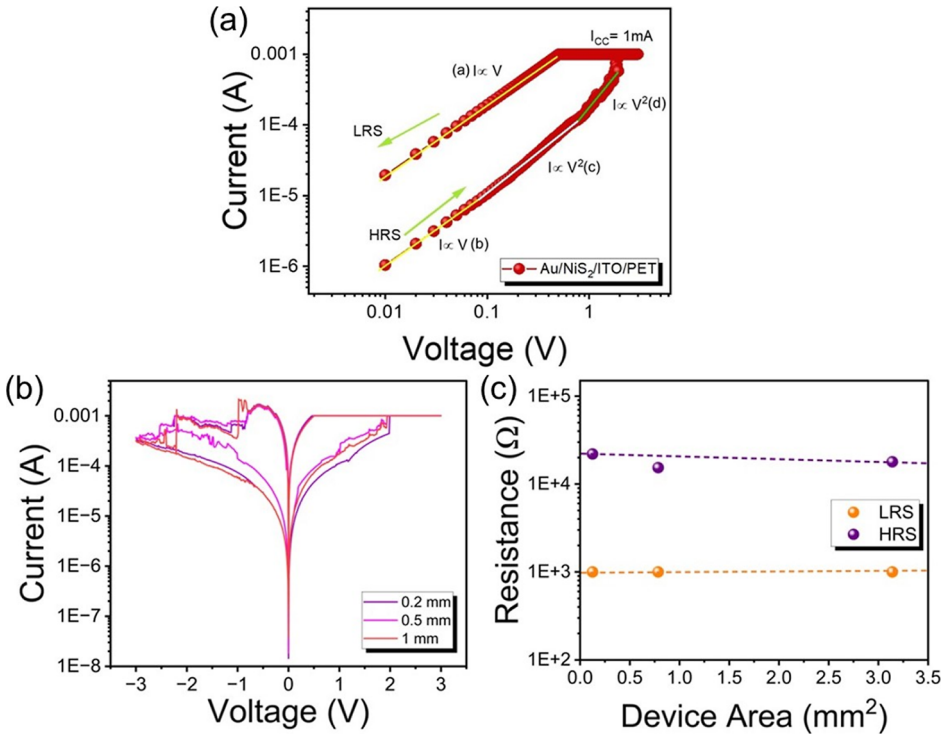

Figure 6. (a) Double logarithmic $I-V$ plot showing charge transport fitting models. (b) Bipolar $I-V$ switching characteristics with varied sizes of top electrode (radius—0.2, 0.5, 1 mm) and (c) HRS and LRS of the flexible Au/NiS2/ITO/PET memristor as the function of device area.

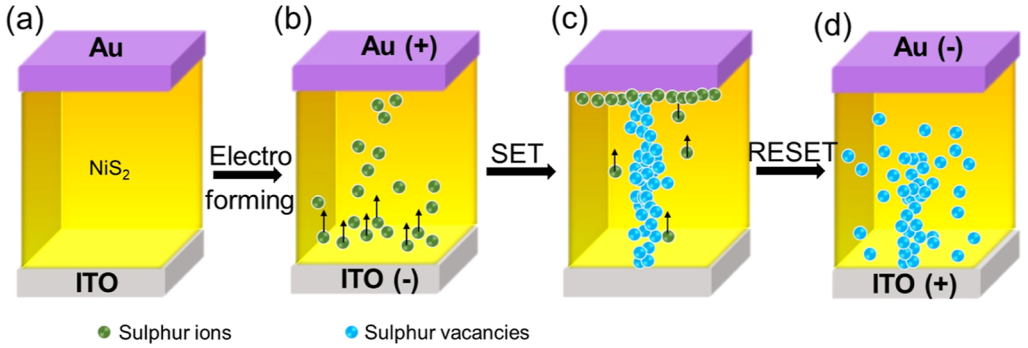

Figure 7. Schematic illustration of switching mechanism of flexible Au/NiS_2/ITO/PET memory device. (a) Pristine state, (b) electroforming process, (c) SET process, and (d) RESET process.

To investigate the conduction mechanism in the Au/NiS_2/ITO/PET memristor, the $I-V$ plot was converted to a double-logarithmic scale, as shown in Figure 6a (elaborated fitting graphs for different regions are mentioned in Figure S6). The conduction mechanism is studied by considering four regions. In the LRS (0−0.5 V), the fitting results indicate the dominance of the Ohmic conduction mechanism where the current is linearly proportional to the applied voltage (region a) and suggest the formation of conductive filament within the switching layer during the SET process. In the case of HRS, the Ohmic conduction is found to be dominated at a low voltage region ($I \propto V$) (region b). This can be attributed to the thermally generated charge carriers taking part in the conduction at a low-applied field.[37] At the mid- and high-voltage regions, the current shows voltage square dependence, hence following Child's square law ($I \propto V^2$) (regions c and d), thus indicating the governance of the space-charge-limited-current (SCLC) conduction model, which is widely observed in most of the low-dimensional materials.[38]

To further elucidate the switching mechanism, we have conducted the top electrode-area-dependent study of our flexible memristor. Figure 6b illustrates the bipolar $I-V$ characteristics of the dot patterned devices with varying areas (radius 0.2, 0.5- and 1 mm). It is worth noting that the devices exhibit similar kinds of $I-V$ curves for each top electrode. Moreover, Figure 6c presents a plot of HRS and LRS with respect to the device area. It is evident that the LRS is independent of the device area and HRS decreases with respect to the increase in area. The remarkable area independence within LRS confirms the filamentary-based switching behavior of the typical ReRAM.[39]

3.4.2. Conduction Mechanism. The RS mechanism of Au/NiS_2/ITO/PET is consistent with the above-mentioned fitting models and the electrical properties of the device. Figure 7a shows the pristine state of the fabricated Au/NiS_2/ITO/PET device. It has been reported that there are numerous sulfur vacancies (V_s) in TMDCs.[40,41] Initially, the high positive biasing greater than the V_{SET} is applied to the device, known as

https://doi.org/10.1021/acsomega.3c06331
ACS Omega 2023, 8, 48873−48883

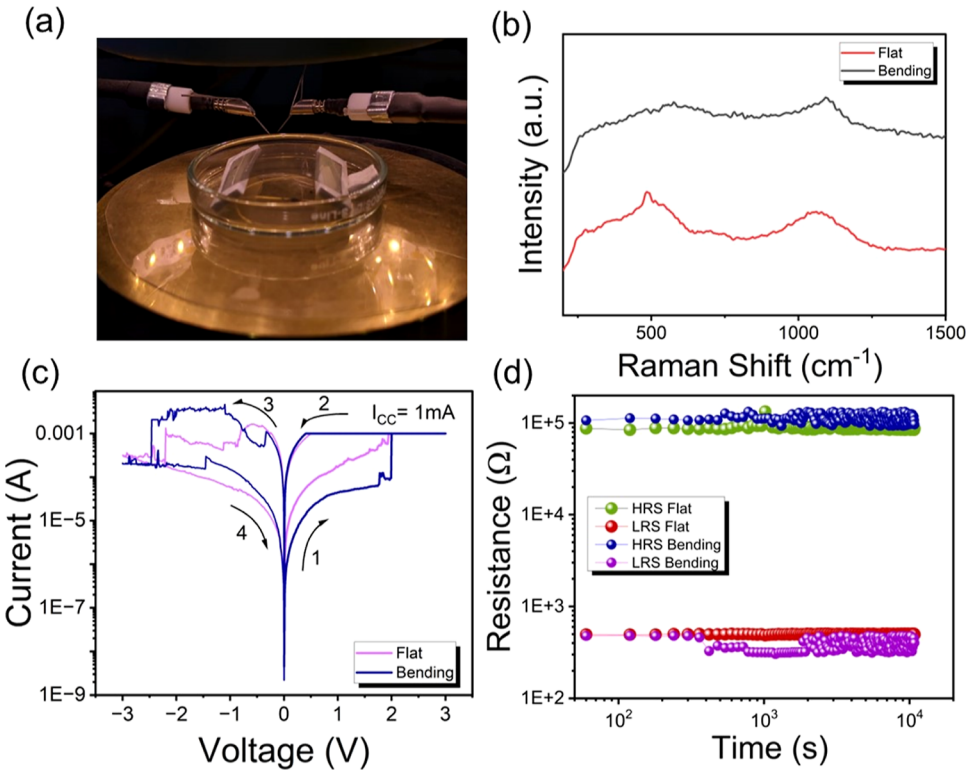

Figure 8. (a) Photograph of flexible Au/NiS_2/ITO/PET for bending test (R = 20 mm). (b) Raman spectra of a flexible device during flat and bending tests. (c) Semilog $I-V$ characteristics and (d) retention performance of the flexible device prior to bending and during bending.

Table 1. TMDC-Based Memristor Devices for Nonvolatile Memory Application

device configuration	fabrication route	switching voltage (V)	retention (s)	flexible	refs
Au/NiS_2/ITO/PET	single-step hydrothermal	±2	10^4	yes	this work
Al/MoS_2-GO/Al	spin coat	+0.3 and −1	10^4	-	47
Al/$MoSe_2$@PMMA/ITO	hydrothermal and spin coat	+1 and −3	10^3	-	48
Al/WS_2/Pt/Ti/SiO_2/Si	CVD	±2	10^3	-	49
Ag/MoS_2/Ag	CVD	+0.8 and −0.6	10^5	-	41
Ag/WO_{3-x}/WSe_2/graphene	mechanical exfoliation	±3	10^3	-	50
Ti/Ni/$MoTe_2$/Ti/Au	mechanical exfoliation	±3	10^2	-	51
Pt/WSe_2/Pt	wet transfer method	±2	10^4	-	52
Ti/MoS_2/Pt	vacuum filtration and transfer	±0.2	10^4	-	44
Ag/MoS_2/Au	exfoliation	±1	10^4	yes	42

the forming voltage which causes the dielectric breakdown in the NiS_2 thin films. During this forming process with positive biasing of the top electrode, the sulfur atoms ionize to S^{2-} ions at the bottom electrode (Figure 7b). The sulfur ions behave as movable anionic species[42] similar to oxygen ion species.[43] Further, when a positive voltage (+3 V) is applied to the top electrode, the S^{2-} ions transfer and accumulate at the top electrode and react with Au to form a conductive layer at the Au/NiS_2 interface. The escaping sulfur ions leave a large number of sulfur vacancies (V_s) behind, eventually forming a conduction filament (CF) connecting the top and bottom electrodes and causing filament formation (Figure 7c).[44] The filament formation switches the device to the LRS, i.e., the SET process. Further, reversing the polarity (−3 V) causes the rupturing of filament and the device switches to an HRS, i.e., RESET process (Figure 7d). The device switches between the ON and OFF states.

3.4.3. Bending Test. To confirm the mechanical feasibility of our device for flexible nonvolatile memory applications and wearable electronics, the device was subjected to a bending radius (R) of 20 mm. The switching performance and Raman stretching modes during flat and bending conditions are shown in Figure 8a,b, respectively. The applied strain was calculated using the below equation[45]

$$\text{strain}(\%) = (\text{total thickness of device}) / (2 \times \text{radius of curvature}) \times 100 \quad (1)$$

where the total thickness of the device is 208.4 μm, consisting of the top electrode (100 nm), NiS_2 layer thickness (8.01 μm), ITO layer (200 nm), and substrate (200 μm), and radius of curvature is 20 mm. The applied strain to the substrate was 0.52%. During bending, the broadening of bands at lower frequencies (i.e., 480 and 513 cm^{-1}) takes place and the vibration frequency decreases which can be attributed to the increase in bond length. Thus, the bending condition causes a slight change in A_{1g} stretching modes leading to broadening and shifting of peak toward the lower frequency values.[46] The device shows bipolar RS during the bending test with reliable

https://doi.org/10.1021/acsomega.3c06331
ACS Omega 2023, 8, 48873−48883

SET and RESET processes at a low operating voltage (Figure 8c). The similar compliance currents of 1 and 50 mA (positive and negative voltage region, respectively) were set to avoid the breakdown of the device. Interestingly, the device exhibited reliable performance under bending conditions with a shift in the ON current toward a higher level. This can be attributed to the polysulfide filament formation maintaining the flexibility within the thin NiS_2 layer.[37] Moreover, the effect is reversible, and the ON current returns to its original position after bending (Figure S7). The retention test of the flexible device was studied to evaluate the stability and reliability of the device under strain. The HRS and LRS were consistent over 10^4 s without degradation under bending conditions indicating the nonvolatility and better performance of the fabricated flexible device (Figure 8d).

Table 1 shows the comparative study of the RS performance of our flexible Au/NiS_2/ITO/PET device with other reported metal-sulfide-based memory devices. It has been observed that the study is limited to the usage of MoS_2, $MoSe_2$, WS_2, and WSe_2 as the switching layer on the rigid substrates. Notably, our device demonstrates single-step and scalable device fabrication along with competitive switching performance onto the flexible substrate. Moreover, the easy stochiometric modulations of the novel precursors enable eco-friendly, low-temperature processing and high throughput production, making it compatible with the thermal budget of the flexible substrates. This prevents the deformation of polymer substrates and paves the way for future large-scale manufacturing of metal-chalcogenide-based thin films, beneficial for the development of flexible and wearable electronics.

4. CONCLUSIONS

In summary, we have successfully demonstrated the simple, solution-processable solvothermal route for *in situ* growth of the nanostructured NiS_2 thin film on a flexible substrate via SSP. This novel low-temperature route negates the key thermal budget requirement for most of the flexible substrates, providing a low-cost, scalable, industrially compatible processing. The as-deposited NiS_2 nanoflowers (~50−100 nm) with dense morphology, high surface area, and negligible surface roughness serve as a suitable platform for RS memory onto a flexible substrate. The fabricated Au/NiS_2/ITO/PET device revealed reliable and reproducible bipolar RS behavior at low operating voltage. Furthermore, the device exhibits data retention up to 10^4 s and a uniform cycle-to-cycle performance over 70 continuous cycles. The detailed study of the conduction mechanism reveals ohmic and SCLC-based device conduction. The switching mechanism is attributed to the formation and rupture of filament based on the migration of sulfur ions and vacancies within the porous structure of the active layer. Moreover, the Au/NiS_2/ITO/PET device successfully demonstrated reliable RS under the applied strain of 0.52% with good mechanical stability and retention properties with well-resolved switching states and a memory window (~100). The cost-effective and scalable nickel disulfide-based flexible device could be a potential candidate for future wearable electronics and next-generation neuromorphic computing applications.

ASSOCIATED CONTENT

Supporting Information

The Supporting Information is available free of charge at https://pubs.acs.org/doi/10.1021/acsomega.3c06331.

Spectroscopic details (FTIR, $\{^1H\}$ and $^{31}P\{^1H\}$ NMR) of $[Ni\{S_2P(OPr)_2\}_2]$ precursor. Additional details of flexible Au/NiS_2/ITO/PET device: transmittance spectra, DC endurance studies, charge transport fitting models over different voltage ranges, and bending reversibility test (PDF)

AUTHOR INFORMATION

Corresponding Author

Chitra Gurnani − *Department of Chemistry, Ecole Centrale School of Engineering, Mahindra University, Hyderabad 500043, India;* orcid.org/0000-0003-2950-7393; Email: chitra.gurnani@mahindrauniversity.edu.in

Authors

Trishala R. Desai − *Department of Chemistry, Ecole Centrale School of Engineering, Mahindra University, Hyderabad 500043, India;* orcid.org/0000-0003-4286-0810

R. Sai Prasad Goud − *Centre for Advanced Studies in Electronic Sciences and Technology, University of Hyderabad, Hyderabad 500046, India;* orcid.org/0000-0003-1533-0582

Tukaram D. Dongale − *Computational Electronics and Nanoscience Research Laboratory, School of Nanoscience and Biotechnology, Shivaji University, Kolhapur 416004, India;* orcid.org/0000-0003-2536-6132

Complete contact information is available at: https://pubs.acs.org/10.1021/acsomega.3c06331

Author Contributions

T. R. Desai: Conceptualization, Methodology, Data curation, Investigation, Validation, Analysis, Writing—Original draft. **R. S. P. Goud**: Electrical characterization and Analysis. **T. D. Dongale**: Electrical characterization, validation, and Analysis **C. Gurnani**: Conceptualization, Methodology, Investigation, Validation, Analysis, Writing—review and editing, Supervision.

Notes

The authors declare no competing financial interest.

ACKNOWLEDGMENTS

The authors thank Mahindra University, Hyderabad for providing the necessary experimental facilities and funding to carry out this work. The authors thank the School of Chemistry, University of Hyderabad for providing FESEM and AFM facilities and UGC-NRC, School of Physics for UV−vis and transmission studies of the films. The authors also thank SAIF Chandigarh for providing NMR facilities.

ABBREVIATIONS

SSP, single-source precursor; PET, polyethylene terephthalate; ITO, indium tin oxide; 2D, two dimensional; RS, resistive switching; HRS, high resistance state; LRS, low resistance state; TE, top electrode; BE, bottom electrode; DC, direct current; SCLC, space-charge-limited-current; CF, conduction filament

REFERENCES

(1) Choi, C.; Lee, Y.; Cho, K. W.; Koo, J. H.; Kim, D. H. Wearable and Implantable Soft Bioelectronics Using Two-Dimensional Materials. *Acc. Chem. Res.* **2019**, *52* (1), 73−81.

(2) Yao, S.; Ren, P.; Song, R.; Liu, Y.; Huang, Q.; Dong, J.; O'Connor, B. T.; Zhu, Y. Nanomaterial-Enabled Flexible and

https://doi.org/10.1021/acsomega.3c06331
ACS Omega 2023, 8, 48873−48883

Stretchable Sensing Systems: Processing, Integration, and Applications. *Adv. Mater.* **2020**, *32* (15), 1902343.
(3) Zhu, B.; Wang, H.; Leow, W. R.; Cai, Y.; Loh, X. J.; Han, M. Y.; Chen, X. Silk Fibroin for Flexible Electronic Devices. *Adv. Mater.* **2016**, *28* (22), 4250−4265.
(4) Chaudhary, V.; Kaushik, A.; Furukawa, H.; Khosla, A. Review—Towards 5th Generation AI and IoT Driven Sustainable Intelligent Sensors Based on 2D MXenes and Borophene. *ECS Sensors Plus* **2022**, *1* (1), 013601.
(5) Mao, R.; Zhang, D.; Wang, Z.; Zhang, H.; Wang, D.; Tang, M.; Zhou, L.; Cai, H.; Xia, H. Deep-Learning-Assisted Low-Cost Flexible Cotton Yarn-Based Triboelectric Nanogenerator for Ultra-Sensitive Human-Computer Merging Interfaces. *Nano Energy* **2023**, *111*, 108418.
(6) Bhattacharyya, A.; Sanyal, M. K.; Mogera, U.; George, S. J.; Mukhopadhyay, M. K.; Maiti, S.; Kulkarni, G. U. In-Situ GISAXS Study of Supramolecular Nanofibers Having Ultrafast Humidity Sensitivity. *Sci. Rep.* **2017**, *7* (1), 246.
(7) Mehonic, A.; Kenyon, A. J. Brain-Inspired Computing Needs a Master Plan. *Nature* **2022**, *604* (7905), 255−260.
(8) Sun, K.; Chen, J.; Yan, X. The Future of Memristors: Materials Engineering and Neural Networks. *Adv. Funct. Mater.* **2021**, *31* (8), 2006773.
(9) Dongale, T. D.; Khot, A. C.; Takaloo, A. V.; Kim, T. G. Facile Synthesis of Nickel Cobaltite Quasi-Hexagonal Nanosheets for Multilevel Resistive Switching and Synaptic Learning Applications. *NPG Asia Mater.* **2021**, *13* (1), 16.
(10) Qian, K.; Cai, G.; Nguyen, V. C.; Chen, T.; Lee, P. S. Direct Observation of Conducting Filaments in Tungsten Oxide Based Transparent Resistive Switching Memory. *ACS Appl. Mater. Interfaces* **2016**, *8* (41), 27885−27891.
(11) Li, X.; Yang, J. G.; Ma, H. P.; Liu, Y. H.; Ji, Z. G.; Huang, W.; Ou, X.; Zhang, D. W.; Lu, H. L. Atomic Layer Deposition of Ga_2O_3/ZnO Composite Films for High-Performance Forming-Free Resistive Switching Memory. *ACS Appl. Mater. Interfaces* **2020**, *12* (27), 30538−30547.
(12) More, S. S.; Patil, P. A.; Kadam, K. D.; Patil, H. S.; Patil, S. L.; Pawar, A. V.; Kanapally, S. S.; Desai, D. V.; Bodake, S. M.; Kamat, R. K.; Kim, S.; Dongale, T. D. Resistive Switching and Synaptic Properties Modifications in Gallium-Doped Zinc Oxide Memristive Devices. *Results Phys.* **2019**, *12*, 1946−1955.
(13) Liang, Q.; Zhang, Q.; Zhao, X.; Liu, M.; Wee, A. T. S. Defect Engineering of Two-Dimensional Transition-Metal Dichalcogenides: Applications, Challenges, and Opportunities. *ACS Nano* **2021**, *15* (2), 2165−2181.
(14) Bauers, S. R.; Tellekamp, M. B.; Roberts, D. M.; Hammett, B.; Lany, S.; Ferguson, A. J.; Zakutayev, A.; Nanayakkara, S. U. Metal Chalcogenides for Neuromorphic Computing: Emerging Materials and Mechanisms. *Nanotechnology* **2021**, *32* (37), 372001.
(15) Bertolazzi, S.; Brivio, J.; Kis, A. Stretching and Breaking of Ultrathin MoS_2. *ACS Nano* **2011**, *5* (12), 9703−9709.
(16) He, H. K.; Yang, F. F.; Yang, R. Flexible Full Two-Dimensional Memristive Synapses of Graphene/$WSe_{2-X}O_y$/Graphene. *Phys. Chem. Chem. Phys.* **2020**, *22* (36), 20658−20664.
(17) Meng, J. L.; Wang, T. Y.; Chen, L.; Sun, Q. Q.; Zhu, H.; Ji, L.; Ding, S. J.; Bao, W. Z.; Zhou, P.; Zhang, D. W. Energy-Efficient Flexible Photoelectric Device with 2D/0D Hybrid Structure for Bio-Inspired Artificial Heterosynapse Application. *Nano Energy* **2021**, *83*, 105815.
(18) Ji, Q.; Zhang, Y.; Zhang, Y.; Liu, Z. Chemical Vapour Deposition of Group-VIB Metal Dichalcogenide Monolayers: Engineered Substrates from Amorphous to Single Crystalline. *Chem. Soc. Rev.* **2015**, *44* (9), 2587−2602.
(19) Novoselov, K. S.; Mishchenko, A.; Carvalho, A.; Castro Neto, A. H. 2D Materials and van Der Waals Heterostructures. *Science* **2016**, *353* (6298), 9439.
(20) Vu, Q. A.; Kim, H.; Nguyen, V. L.; Won, U. Y.; Adhikari, S.; Kim, K.; Lee, Y. H.; Yu, W. J. A High-On/Off-Ratio Floating-Gate Memristor Array on a Flexible Substrate via CVD-Grown Large-Area 2D Layer Stacking. *Adv. Mater.* **2017**, *29* (44), 1703363.
(21) Guiot, V.; Janod, E.; Corraze, B.; Cario, L. Control of the Electronic Properties and Resistive Switching in the New Series of Mott Insulators $GaTa_4Se_{8-Y}Te_y$ ($\leq y \leq 6.5$). *Chem. Mater.* **2011**, *23* (10), 2611−2618.
(22) Bobinihi, F. F.; Fayemi, O. E.; Onwudiwe, D. C. Synthesis, Characterization, and Cyclic Voltammetry of Nickel Sulphide and Nickel Oxide Nanoparticles Obtained from Ni(II) Dithiocarbamate. *Mater. Sci. Semicond. Process.* **2021**, *121*, 105315.
(23) Mi, L.; Ding, Q.; Chen, W.; Zhao, L.; Hou, H.; Liu, C.; Shen, C.; Zheng, Z. 3D Porous Nano/Micro Nickel Sulfides with Hierarchical Structure: Controlled Synthesis, Structure Characterization and Electrochemical Properties. *Dalton Trans.* **2013**, *42* (16), 5724−5730.
(24) Ningrum, V. P.; Liu, B.; Wang, W.; Yin, Y.; Cao, Y.; Zha, C.; Xie, H.; Jiang, X.; Sun, Y.; Qin, S.; Chen, X.; Qin, T.; Zhu, C.; Wang, L.; Huang, W. Recent Advances in Two-Dimensional Magnets: Physics and Devices towards Spintronic Applications. *Research* **2020**, *2020*, 1768918.
(25) Luo, S.; Yang, M.; Li, J.; Wu, Y. One-Step Potentiostatic Electrodeposition of NiS-NiS_2 on Sludge-Based Biochar and Its Application for a Non-Enzymatic Glucose Sensor. *RSC Adv.* **2023**, *13* (9), 5900−5907.
(26) Wadia, C.; Alivisatos, A. P.; Kammen, D. M. Materials Availability Expands the Opportunity for Large-Scale Photovoltaics Deployment. *Environ. Sci. Technol.* **2009**, *43* (6), 2072−2077.
(27) Bingham, A. L.; Drake, J. E.; Gurnani, C.; Hursthouse, M. B.; Light, M. E.; Nirwan, M.; Ratnani, R. Triethyl Ammonium Salt of O,O′-Bis(p-Tolyl)Dithiophosphate, $[Et_3NH]^+[(4\text{-}MeC_6H_4O)_2PS_2]^-$. *J. Chem. Crystallogr.* **2006**, *36* (10), 627−630.
(28) Sathiyaraj, E.; Thirumaran, S. Structural, Morphological and Optical Properties of Iron Sulfide, Cobalt Sulfide, Copper Sulfide, Zinc Sulfide and Copper-Iron Sulfide Nanoparticles Synthesized from Single Source Precursors. *Chem. Phys. Lett.* **2020**, *739*, 136972.
(29) Ghafarian-Zahmatkesh, H.; Javanbakht, M.; Ghaemi, M. Ethylene Glycol-Assisted Hydrothermal Synthesis and Characterization of Bow-Tie-like Lithium Iron Phosphate Nanocrystals for Lithium-Ion Batteries. *J. Power Sources* **2015**, *284*, 339−348.
(30) Wan, Z.; Jia, C.; Wang, Y. In Situ Growth of Hierarchical NiS_2 Hollow Microspheres as Efficient Counter Electrode for Dye-Sensitized Solar Cell. *Nanoscale* **2015**, *7* (29), 12737−12742.
(31) Suzuki, T.; Uchinokura, K.; Sekine, T.; Matsuura, E. Raman Scattering of NiS_2. *Solid State Commun.* **1977**, *23*, 847−852.
(32) Krishnamoorthy, D.; Prakasam, A. Low-Cost and Novel Preparation of Porous NiS_2/Graphene Heterojunctions Photoanodes for High-Efficiency Dye-Sensitized Solar Cells. *Inorg. Chem. Commun.* **2020**, *119*, 108063.
(33) Yoshikawa, M.; Murakami, M.; Matsuda, K.; Matsunobe, T.; Sugie, S.; Okada, K.; Ishida, H. Characterization of Si Nano-Polycrystalline Films at the Nanometer Level Using Resonant Raman Scattering. *J. Appl. Phys.* **2005**, *98* (6), 063531.
(34) Makuła, P.; Pacia, M.; Macyk, W. How To Correctly Determine the Band Gap Energy of Modified Semiconductor Photocatalysts Based on UV-Vis Spectra. *J. Phys. Chem. Lett.* **2018**, *9* (23), 6814−6817.
(35) Sathiyaraj, E.; Gurumoorthy, G.; Thirumaran, S. Nickel(II) Dithiocarbamate Complexes Containing the Pyrrole Moiety for Sensing Anions and Synthesis of Nickel Sulfide and Nickel Oxide Nanoparticles. *New J. Chem.* **2015**, *39* (7), 5336−5349.
(36) Jaafar, A. H.; Meng, L.; Zhang, T.; Guo, D.; Newbrook, D.; Zhang, W.; Reid, G.; De Groot, C. H.; Bartlett, P. N.; Huang, R. Flexible Memristor Devices Using Hybrid Polymer/Electrodeposited GeSbTe Nanoscale Thin Films. *ACS Appl. Nano Mater.* **2022**, *5* (12), 17711−17720.
(37) Perla, V. K.; Ghosh, S. K.; Mallick, K. Ultrafine Nickel Sulfide-Based Bipolar Resistive Switching Device as Artificial Synapses for Neuromorphic Application. *ACS Appl. Electron. Mater.* **2022**, *4* (12), 6117−6124.

https://doi.org/10.1021/acsomega.3c06331
ACS Omega 2023, 8, 48873−48883

(38) Lim, E. W.; Ismail, R. Conduction Mechanism of Valence Change Resistive Switching Memory: A Survey. *Electronics* **2015**, *4* (3), 586−613.
(39) Kim, W.; Yoo, C.; Park, E. S.; Ha, M.; Jeon, J. W.; Kim, G. S.; Woo, K. S.; Lee, Y. K.; Hwang, C. S. Electroforming-Free Bipolar Resistive Switching in GeSe Thin Films with a Ti-Containing Electrode. *ACS Appl. Mater. Interfaces* **2019**, *11* (42), 38910−38920.
(40) Li, H.; Tsai, C.; Koh, A. L.; Cai, L.; Contryman, A. W.; Fragapane, A. H.; Zhao, J.; Han, H. S.; Manoharan, H. C.; Abild-Pedersen, F.; Nørskov, J. K.; Zheng, X. Activating and Optimizing MoS_2 Basal Planes for Hydrogen Evolution through the Formation of Strained Sulphur Vacancies. *Nat. Mater.* **2016**, *15* (1), 48−53.
(41) Wang, K.; Li, L.; Zhao, R.; Zhao, J.; Zhou, Z.; Wang, J.; Wang, H.; Tang, B.; Lu, C.; Lou, J.; Chen, J.; Yan, X. A Pure 2H-MoS_2 Nanosheet-Based Memristor with Low Power Consumption and Linear Multilevel Storage for Artificial Synapse Emulator. *Adv. Electron. Mater.* **2020**, *6* (3), 1901342.
(42) Zhao, X.; Fan, Z.; Xu, H.; Wang, Z.; Xu, J.; Ma, J.; Liu, Y. Reversible Alternation between Bipolar and Unipolar Resistive Switching in Ag/MoS_2/Au Structure for Multilevel Flexible Memory. *J. Mater. Chem. C* **2018**, *6* (27), 7195−7200.
(43) Yang, Y.; Zhang, X.; Qin, L.; Zeng, Q.; Qiu, X.; Huang, R. Probing Nanoscale Oxygen Ion Motion in Memristive Systems. *Nat. Commun.* **2017**, *8*, 15173.
(44) Liu, L.; Wang, Y.; Chen, W.; Ren, S.; Guo, J.; Kang, X.; Zhao, X. Robust Resistive Switching in MoS_2-Based Memristor with Ti Top Electrode. *Appl. Surf. Sci.* **2022**, *605*, 154698.
(45) Ji, Y.; Yang, Y.; Lee, S. K.; Ruan, G.; Kim, T. W.; Fei, H.; Lee, S. H.; Kim, D. Y.; Yoon, J.; Tour, J. M. Flexible Nanoporous WO_{3-x} Nonvolatile Memory Device. *ACS Nano* **2016**, *10* (8), 7598−7603.
(46) Bissett, M. A.; Tsuji, M.; Ago, H. Strain Engineering the Properties of Graphene and Other Two-Dimensional Crystals. *Phys. Chem. Chem. Phys.* **2014**, *16* (23), 11124−11138.
(47) Choudhary, S.; Soni, M.; Sharma, S. K. Low voltage & controlled switching of MoS_2-GO resistive layers-based ReRAM for non-volatile memory applications. *Semicond. Sci. Technol.* **2019**, *34* (8), 085009.
(48) Das, B.; Bera, A.; Samanta, M.; Bera, S.; Kalimuddin, S.; Kundu, M.; Gayen, S.; Chattopadhyay, K. K.; Mondal, M. Resistive Switching in a $MoSe_2$-Based Memory Device Investigated Using Conductance Noise Spectroscopy. *ACS Appl. Electron. Mater.* **2021**, *3* (7), 3096−3105.
(49) Das, U.; Bhattacharjee, S.; Mahato, B.; Prajapat, M.; Sarkar, P.; Roy, A. Uniform, Large-Scale Growth of WS_2 Nanodomains via CVD Technique for Stable Non-volatile RRAM Application. *Mater. Sci. Semicond. Process.* **2020**, *107*, 104837.
(50) Huh, W.; Jang, S.; Lee, J. Y.; Lee, D.; Lee, D.; Lee, J. M.; Park, H.-G.; Kim, J. C.; Jeong, H. Y.; Wang, G.; Lee, C.-H. Synaptic Barristor Based on Phase-Engineered 2D Heterostructures. *Adv. Mater.* **2018**, *30* (35), 1801447.
(51) Zhang, F.; Zhang, H.; Krylyuk, S.; Milligan, C. A.; Zhu, Y.; Zemlyanov, D. Y.; Bendersky, L. A.; Burton, B. P.; Davydov, A. V.; Appenzeller, J. Electric-Field Induced Structural Transition in Vertical $MoTe_2$ and $Mo_{1-x}W_xTe_2$ -Based Resistive Memories. *Nat. Mater.* **2019**, *18* (1), 55−61.
(52) Cheng, S.; Zhong, L.; Yin, J.; Duan, H.; Xie, Q.; Luo, W.; Jie, W. Controllable Digital and Analog Resistive Switching Behavior of 2D Layered WSe_2 Nanosheets for Neuromorphic Computing. *Nanoscale* **2023**, *15*, 4801−4808.

https://doi.org/10.1021/acsomega.3c06331
ACS Omega 2023, 8, 48873−48883